

Revisiting the envelope approximation: gravitational waves from bubble collisions

David J. Weir^{1,*}

¹ *Institute of Mathematics and Natural Sciences,
University of Stavanger, 4036 Stavanger, Norway*

(Dated: June 15, 2016)

We study the envelope approximation and its applicability to first-order phase transitions in the early universe. We demonstrate that the power laws seen in previous studies exist independently of the nucleation rate. We also compare the envelope approximation prediction to results from large-scale phase transition simulations. For phase transitions where the contribution to gravitational waves from scalar fields dominates over that from the coupled plasma of light particles, the envelope approximation is in agreement, giving a power spectrum of the same form and order of magnitude. In all other cases the form and amplitude of the gravitational wave power spectrum is markedly different and new techniques are required.

PACS numbers: 64.60.Q-, 04.30.-w, 03.50.-z, 95.30.Lz

I. INTRODUCTION

With the upgrades of the LIGO and VIRGO gravitational wave observatories [1, 2], it was only a matter of time before an astrophysical source of gravitational waves was detected [3]. Cosmological sources of gravitational waves also exist, and their detection would offer an exciting new tool to study the physics of the early universe. Proposals for several space-based gravitational wave detectors are under development, with sensitivities sufficient to detect cosmological sources of gravitational waves. In particular, eLISA is scheduled for launch in 2034 and offers a realistic prospect of detecting gravitational waves from cosmological sources [4], including first-order phase transitions [5].

There has long been interest in the expected gravitational wave power spectrum produced by a first-order phase transition at, for example, the electroweak scale [6–14]. There is also a growing body of more recent work aimed at making predictions for other scenarios where a first-order phase transition may be detectable [15–17].

Early studies modelled the process as the collision of thin shells of stress-energy, initially for vacuum transitions [18, 19] and then later for thermal transitions [6]. Further refinements in Ref. [9] have set the state of the art and produced a robust form of the power spectrum that has been widely adopted in the literature when making predictions. For thermal phase transitions, there is good understanding of how much energy ends up in the plasma of light particles around the bubble wall [20]. The set of simplifying assumptions going into these thin-shell calculations is usually termed the envelope approximation. While the power spectrum must be computed numerically in the envelope approximation, there is some analytical understanding of the process as well [21–23].

Meanwhile, progress has also been made in understanding other mechanisms giving rise to gravitational

waves after first-order phase transitions. These include turbulence [24–26] and acoustic waves in the plasma of light particles [27–29]. In particular, the acoustic wave source produces a dramatically different power spectrum form with potentially much greater amplitude than predicted by the envelope approximation. As of yet, no analytic calculation can reproduce the results of Refs. [27–29], in which the acoustic behaviour was explored primarily through simulations of a coupled field-fluid model.

In Ref. [9], the power spectrum from the envelope approximation was parametrised as

$$\Omega_{\text{GW}}^{\text{env}}(\omega) = \tilde{\Omega}_{\text{GW}}^{\text{env}} \frac{(a+b)\tilde{\omega}^b \omega^a}{b\tilde{\omega}^{(a+b)} + a\omega^{(a+b)}}, \quad (1)$$

with peak frequency $\tilde{\omega}$, peak amplitude $\tilde{\Omega}_{\text{GW}}^{\text{env}}$, and two power-law exponents $a \in [2.66, 2.82]$ and $b \in [0.90, 1.19]$. The fraction of energy in gravitational waves was found to be

$$\tilde{\Omega}_{\text{GW}}^{\text{env}} \simeq \frac{0.11 v_w^3}{0.42 + v_w^2} \left(\frac{H_*}{\beta} \right)^2 \frac{\kappa^2 \alpha_T^2}{(\alpha_T + 1)^2}. \quad (2)$$

Here, v_w is the wall velocity, κ is the efficiency factor gauging what fraction of vacuum energy ends up contributing to the stress-energy localised at the bubble wall, and α_T is the ratio of latent heat to radiation. The ratio H_*/β determines how quickly the transition proceeds: β is the nucleation rate and H_* is the Hubble rate at the time of the transition.

In the calculations leading to the above expressions it was assumed that the fluid kinetic energy was localised near the bubble wall, whereas in reality it reaches a scaling profile proportional to the bubble radius, meaning that the assumption of thin shells instantaneously colliding does not hold (see Fig. 1). Furthermore, the fluid kinetic energy persists as sound waves in the plasma after the transition, until turbulence and expansion attenuate this source.

In Ref. [29], it was argued that the actual energy deposited in gravitational waves by a fluid source is approx-

*Electronic address: david.weir@uis.no

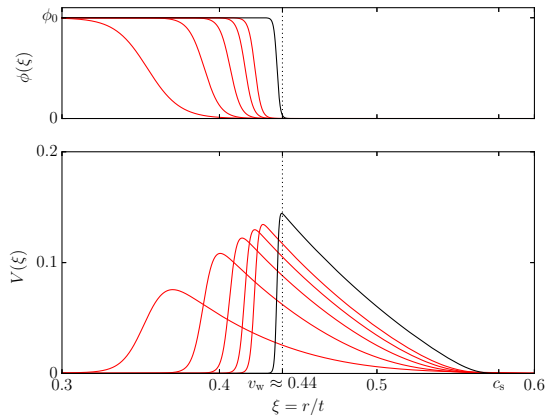


FIG. 1: Plot comparing (top) the radial field $\phi(\xi)$ and (bottom) fluid velocity $V(\xi)$ profiles for the ‘weak’ parameters, as a function of $\xi = r/t$ (the parameters can be found in Table I). A weak deflagration with $v_w \approx 0.44$ is shown. The development of the profiles is illustrated by the red curves (at time intervals of $500/T_c$ up to $2500/T_c$), while the profile at $5000/T_c$ is shown in black. The scalar field bubble wall remains of constant width, while the fluid profile approaches a scaling solution, and is of thickness $\sim |v_w - c_s| R_*/v_w$ when bubbles of radius R_* collide. The envelope approximation of thin colliding shells might therefore be expected to work for scalar field walls, but plainly cannot for colliding fluid shocks unless $v_w \approx c_s$.

imately

$$\tilde{\Omega}_{\text{GW}}^{\text{sound}} \simeq 3(\kappa\alpha_T)^2 \left(H_* (8\pi)^{\frac{1}{3}} \frac{v_w}{\beta} \right) \tilde{\Omega}_{\text{GW}}^{\text{env}} \quad (3)$$

– typically a factor $60(\beta/H_*)$ larger than the envelope approximation result. The power spectrum of gravitational waves was also very different.

Therefore, the envelope approximation should not be used to fully describe phase transitions where a lot of kinetic energy ends up in the fluid. It may still remain valid for gravitational waves sourced by the collision of scalar field bubble walls, which do not scale. It may also model the initial collision of the fluid shells, if they are thin enough, such as in Jouguet detonations.

The various types of sources – scalar field collisions, fluid shell collisions, acoustic waves and turbulence – contribute to different extents, depending on the model.

The principal aim of this paper is to directly test the envelope approximation against a full lattice simulation for the first time, concentrating on the scalar field bubble walls in a thermal phase transition. This is motivated by two observations. First, collisions of the scalar field walls will always source gravitational waves (although the source may well be subdominant for a thermal phase transition). Second, in certain cases, such as where the wall runs away, scalar field collisions may be the dominant source of gravitational waves.

We will also investigate the suitability of the enve-

lope approximation result for modelling the production of gravitational waves by colliding plasma shells. Immediately after the shells have collided, it does get the amplitude of gravitational waves approximately right, but the high-frequency and long-term behaviour of the gravitational wave power spectrum are both incorrect.

In Section II we review the production of gravitational waves by bubble collisions in the formalism of Ref. [30], and the approximations involved. Next, in Section III we give details of our numerical evaluation of the envelope approximation, and present the comparison of our results to those obtained previously.

The techniques used in direct numerical lattice simulations of the phase transition are reprised in Section IV, and comparisons with the envelope approximation are made. We discuss the results in Section V.

II. PRODUCTION OF GRAVITATIONAL RADIATION

The quantity of interest is typically the fraction of energy emitted as gravitational waves per decade,

$$\Omega_{\text{GW}} = \omega \frac{dE_{\text{GW}}}{d\omega} \frac{1}{E_{\text{tot}}} \equiv \frac{dE_{\text{GW}}}{d \ln \omega} \frac{1}{E_{\text{tot}}} \quad (4)$$

where E_{tot} is the total energy.

The gravitational wave power radiated in a direction $\hat{\mathbf{k}}$ at a frequency ω per unit solid angle Ω is [30]

$$\frac{dE_{\text{GW}}}{d\Omega d\omega} = 2G\omega^2 \Lambda_{ij,lm}(\hat{\mathbf{k}}) \tau_{ij}^*(\hat{\mathbf{k}}, \omega) \tau_{lm}(\hat{\mathbf{k}}, \omega), \quad (5)$$

where $\Lambda_{ij,lm}$ is the projection tensor

$$\begin{aligned} \Lambda_{ij,lm}(\hat{\mathbf{k}}) \equiv & \delta_{il}\delta_{jm} - 2\hat{\mathbf{k}}_j\hat{\mathbf{k}}_m\delta_{ij} + \frac{1}{2}\hat{\mathbf{k}}_i\hat{\mathbf{k}}_j\hat{\mathbf{k}}_l\hat{\mathbf{k}}_m \\ & - \frac{1}{2}\delta_{ij}\delta_{lm} + \frac{1}{2}\delta_{ij}\hat{\mathbf{k}}_l\hat{\mathbf{k}}_m + \frac{1}{2}\delta_{lm}\hat{\mathbf{k}}_i\hat{\mathbf{k}}_j; \end{aligned} \quad (6)$$

and $\tau_{ij}(\hat{\mathbf{k}}, \omega)$ is the Fourier transformed stress-energy tensor

$$\tau_{ij}(\hat{\mathbf{k}}, \omega) = \frac{1}{2\pi} \int dt e^{i\omega t} \int d^3x e^{-i\omega\hat{\mathbf{k}}\cdot\mathbf{x}} \tau_{ij}(\mathbf{x}, t). \quad (7)$$

For a scalar field ϕ , the source is given by

$$\tau_{ij}^{\phi} = \partial_i\phi\partial_j\phi \quad (8)$$

while for a relativistic fluid with energy ϵ , pressure p , relativistic gamma factor W and 3-velocity V_i , the source is

$$\tau_{ij}^{\text{f}} = W^2(\epsilon + p)V_iV_j \quad (9)$$

(the pieces proportional to the metric in the full stress-energy tensor are pure trace and hence do not source gravitational waves).

In addition to the linearised gravity approximation that yields the above expressions, two further simplifications are usually employed when computing the resulting gravitational wave power [19]. First, the collided portions of the bubbles are neglected; this is what is *most strictly* described as the envelope approximation. Second, the bubble walls are treated as sufficiently thin that the oscillatory part of the integral $e^{-i\omega\hat{\mathbf{k}}\cdot\mathbf{x}}$ is approximately constant in the region where τ_{ij} is nonzero.

The combination of the above approximations (often collectively referred to simply as the ‘envelope approximation’) has also been applied to thermal phase transitions, where the scalar field is coupled to a number of degrees of freedom that form a plasma [6]. One can compute an efficiency factor κ^f for the conversion of vacuum energy into plasma kinetic energy [6, 20], and if one assumes that the shell of fluid is thin then the envelope approximation can be adapted to this case [9].

The resulting simple prediction of a broken power law form for the power spectrum from gravitational waves at a first-order phase transition has been widely adopted in the literature (see for example Refs. [11, 12, 15, 31]): an approximately ω^3 dependence at low frequencies, and an approximately ω^{-1} dependence at high frequencies. The break occurs at a characteristic length scale, believed to be set by ratio of the inverse nucleation rate to the Hubble rate (H_*/β). Heuristically, the ω^3 dependence can be seen as the absence of structure (‘white noise’) on longer length scales, while it has been argued that the approximate ω^{-1} dependence at short length scales can be attributed to the size distribution of bubbles. In the following section we will show that both power laws are intrinsic features of the set of approximations outlined above, irrespective of whether the bubbles are nucleated simultaneously or with a physically-motivated exponential rate.

The collision of a pair of scalar field bubbles was treated numerically in Ref. [18]. Since then, there have not been any further attempts to perform direct numerical simulations that compare the envelope approximation with dynamical vacuum scalar fields or field-fluid systems modelling thermal phase transitions. In Refs. [27, 29], a transient ω^{-1} power law was seen for the gravitational wave power spectrum at early times, which was attributed to the scalar field collisions. This assertion shall be tested in the present work.

III. COMPUTATIONS IN THE ENVELOPE APPROXIMATION

The envelope approximation consists of approximating the stress-energy of the bubble wall with an infinitesi-

mally thin shell, yielding

$$\tau_{ij}(\hat{\mathbf{k}}, \omega) = \kappa \rho_{\text{vac}} v_b^3 C_{ij}(\hat{\mathbf{k}}, \omega) \quad (10)$$

$$C_{ij}(\hat{\mathbf{k}}, \omega) = \frac{1}{6\pi} \sum_n \int dt e^{i\omega(t-\hat{\mathbf{k}}\cdot\mathbf{x}_n)(t-t_n^3)} A_{n,ij}(\mathbf{k}, \omega) \quad (11)$$

$$A_{n,ij}(\hat{\mathbf{k}}, \omega) = \int_{S_n} d\Omega e^{-i\omega v_b(t-t_n)\hat{\mathbf{k}}\cdot\hat{\mathbf{x}}_i\hat{\mathbf{x}}_j}. \quad (12)$$

If the source under study is a system of intersecting fluid shells, then the efficiency factor $\kappa = \kappa^f$ can be computed according to the procedure in Ref. [20]. For scalar field bubble walls, an effective scalar field efficiency factor κ^ϕ can be calculated from the energy density on the bubble walls and the surface area of the bubbles.

We evaluate Eqs. (10-12) using the method given in Ref. [9]. By choosing a system of cylindrical coordinates such that $\hat{\mathbf{k}}$ is aligned with the z -axis, the projected stress-energy tensor becomes

$$\Lambda_{ij,lm}\tau_{ij}^*\tau_{lm} = \frac{1}{2}(\tau_{xx}^* - \tau_{yy}^*)(\tau_{xx} - \tau_{yy}) + \tau_{xy}^*\tau_{xy} + \tau_{yx}^*\tau_{yx}, \quad (13)$$

and the integrations over C_{ij} and A_{ij} become much simpler. We need simply compute

$$C_{\pm}(\omega) = \frac{1}{6\pi} \sum_n^{N_b} \int dt e^{i\omega(t-z_n)} (t-t_n)^3 A_{n,\pm}(\omega, t) \quad (14)$$

$$A_{n,\pm}(\omega, t) = \int_{-1}^1 dz e^{-iv_b\omega(t-t_n)z} B_{n,\pm}(z, t) \quad (15)$$

where

$$B_{n,+}(z, t) = \frac{(1-z^2)}{2} \int_{S'_n} d\phi \cos(2\phi), \quad (16)$$

$$B_{n,-}(z, t) = \frac{(1-z^2)}{2} \int_{S'_n} d\phi \sin(2\phi). \quad (17)$$

See the appendix of Ref. [9] for more details. The summation over n is a sum over all N_b bubbles in the simulation volume, and the integration region S'_n is the area on the surface of the n th bubble that does not intersect with any other bubble.

To compute the envelope approximation for a fixed volume we not only simulate the bubbles within the volume, but also follow the development of bubbles in adjacent boxes (see Fig. 2). We impose periodic boundary conditions on our box, so we nucleate image bubbles in adjacent boxes. These do not contribute to the power but are included in the evaluation of the unc collided bubble regions. This is in contrast to Refs. [9, 19], where a spherical volume is used, but has the advantage that we can make truly direct comparisons with lattice simulations. This means we must consider the interactions of up to

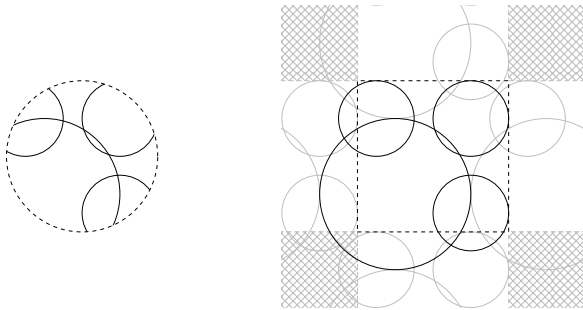


FIG. 2: Bubble geometries used in envelope approximation simulations. At left is the widely adopted spherical cutoff, where all gravitational wave power beyond a certain distance from the ‘central’ bubble is ignored. At right is the ‘mirror’ approach taken in the present work, where image bubbles are nucleated in neighbouring repeating unit cells; the aim of this is to closely model the periodic boundary conditions of lattice simulations. For a sufficiently large number of bubbles the two approaches are equivalent, corresponding to a system with ‘mirror’ boundary conditions.

$27N_b - 1$ other bubbles when determining the contribution of the n th bubble to the total power, although in practice the number of bubbles in range is much smaller.

Our approach to computing the envelope approximation is therefore about an order of magnitude more computationally intensive than previous studies although the number of bubbles participating is around the same. For comparisons with coupled field-fluid simulations, this is not an issue as the dynamic range available there is a more pressing constraint.

The fitted broken power law ansatz for the envelope approximation was given in Eq. (1) – a positive power law with index a at low wavenumber and a negative power law with b at high wavenumber. This also describes our own computations with the envelope approximation and so curves given by fits to Eq. 1 will be shown alongside our simulation results in the following sections.

The theoretical expectation is that the low-frequency rising power law has index $a = 3$, due to causality – there is nothing in the system on length scales larger than the largest bubble, so a cubic power law is anticipated (two powers of ω from the radial integral, and one additional power). We have confirmed this in our envelope approximation simulations.

For the high-frequency power law, it is widely expected that $b \approx 1$, either due to the size distribution of bubbles or intrinsic effects. Unfortunately, we cannot reach high enough frequencies ω to verify that b is exactly unity.

However, we will show that these exponents are intrinsic to the envelope approximation and do not depend on, for example, nucleation rate. Later, we will also show that colliding scalar field bubble walls give the same power laws.

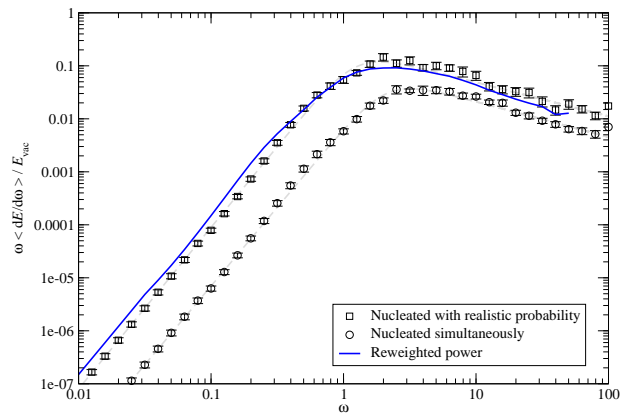


FIG. 3: Comparison of scaled bubble collision power spectra, with $v_w = 1$. We show results from a simulation of 109 bubbles nucleated using the exponentially increasing nucleation rate (squares) and from one where the same number of bubbles are nucleated in the same positions simultaneously (circles). The parameters are such that comparison with Fig. 2 of Ref. [9] is also possible, where the bubbles were nucleated at unequal times but with a spherical boundary to the simulation volume. As expected, there is no dependence on the form of the simulation volume. Furthermore, the unequal nucleation time case can be recovered from the equal nucleation time case by the reweighting outlined in the main text (solid blue curve).

A. Testing the envelope approximation: geometry and nucleation rate

It is standard to model the nucleation probability per unit volume and time P by

$$P = P_0 e^{\beta(t-t_0)}, \quad (18)$$

with β computed, in principle, from the bounce action [32–35]. We instead take β to be a constant numerical value throughout our simulations in this section (in some cases we make it effectively infinite: we nucleate bubbles simultaneously).

In this section, we consider the results of simulations with $v_w = 1$, 109 bubbles and $\beta = 1$ or $\beta \rightarrow \infty$. For a given bubble distribution, our results are the average of 32 uniformly distributed random choices of the z -axis in Eq. (13).

In Fig. 3, we choose a single spatial distribution of bubbles and nucleate them either over time with rate parametrised by the ‘realistic’ $\beta = 1$, or simultaneously. For this bubble distribution, a bootstrapped fit to Eq. (1) for $\omega \in [0.01, 100]$ yields $a = 3.05 \pm 0.03$, $b = 0.62 \pm 0.05$ for the ‘realistic’ case. For the simultaneous case, we obtain $a = 2.98 \pm 0.02$ and $b = 0.65 \pm 0.04$. The power laws at high frequencies in the envelope approximation are therefore not dependent on the size distribution of bubbles at the end of the phase transition.

We have confirmed that these fitted power laws do not change substantially when averaged over eight different bubble distributions.

We can do even more with the simultaneously nucleated simulation. The resulting power spectrum can be rescaled to give the gravitational wave power spectrum for a physical nucleation rate. Given Eq. (5), we can write the rescaled gravitational wave power as

$$\omega \frac{dE_{\text{GW}}}{d\omega} = \omega \sum_n^{N_b} \frac{v_w^3 (t_{\text{end}} - t_{0,n})^3}{\mathcal{V}} \times 2G\tilde{\omega}_n^2 \lambda_{ij,lm}(\hat{\mathbf{k}}) \tau_{ij}^*(\hat{\mathbf{k}}, \tilde{\omega}_n) \tau_{lm}(\hat{\mathbf{k}}, \tilde{\omega}_n) \quad (19)$$

with

$$\tilde{\omega}_n = \frac{v_w (t_{\text{end}} - t_{0,n})}{(\mathcal{V}/N_b)^{1/3}} \omega, \quad (20)$$

where \mathcal{V} is the volume and the summation is over each bubble, the n th bubble being nucleated at time $t_{0,n}$, the phase transition ends at around t_{end} . The numerator is therefore the approximate radius of the n th bubble, while the denominator $(\mathcal{V}/N_b)^{1/3}$ is the average bubble radius in the simulation where all bubbles were nucleated simultaneously. For concreteness, we measure the remaining exposed surface area as a function of time and take t_{end} as the time when the surface area of uncollided bubbles is less than 1% of its peak value.

The result of applying this rescaling is also shown in Fig. 3, with good agreement. A similar rescaling argument would presumably apply to the acoustic source in Ref. [29]. As the bubbles collide at different times, fixing t_{end} is an oversimplification, but it works surprisingly well.

In summary, then, it is clear that the power laws seen in the envelope approximation are an intrinsic feature of the calculation, rather than the distribution of bubbles. It is also possible to reweight gravitational wave power spectra produced at equal times to more realistic distributions.

IV. DIRECT SIMULATIONS OF THE FIELD-FLUID SYSTEM

Having performed some tests of our new envelope approximation code against the existing envelope approximation literature, we now wish to make a comparison against the power spectra provided by lattice simulations.

The equations and parameter choices we use have been discussed extensively elsewhere [27, 29, 36–41], so we present only a brief summary here. We are working with a coupled system of a relativistic ideal fluid U^μ and scalar field ϕ , with energy-momentum tensor

$$T^{\mu\nu} = \partial^\mu \phi \partial^\nu \phi - \frac{1}{2} g^{\mu\nu} (\partial\phi)^2 + [\epsilon + p] U^\mu U^\nu + g^{\mu\nu} p, \quad (21)$$

where the metric is $g^{\mu\nu} = \text{diag}(-1, 1, 1, 1)$. The system has an effective potential

$$V(\phi, T) = \frac{1}{2} \gamma (T^2 - T_0^2) \phi^2 - \frac{1}{3} \alpha T \phi^3 + \frac{1}{4} \lambda \phi^4, \quad (22)$$

	Weak	Weak (scaled)	Intermediate
T_0/T_c	$1/\sqrt{2}$	$1/\sqrt{2}$	$1/\sqrt{2}$
γ	1/18	4/18	2/18
α	$\sqrt{10}/72$	$\sqrt{10}/9$	$\sqrt{10}/72$
λ	10/648	160/648	5/648

TABLE I: Potential parameters used for this paper. These are the same as for Refs. [27, 29]. The ‘weak scaled’ parameters give the same phase transition strength as the ‘weak’ parameters, but the bubble wall width is halved (see Table II).

with parameters given in Table I. The equation of state is

$$\epsilon(T, \phi) = 3aT^4 + V(\phi, T) - T \frac{\partial V}{\partial T}, \quad (23)$$

$$p(T, \phi) = aT^4 - V(\phi, T), \quad (24)$$

$a = (\pi^2/90)g_*$; we take $g_* = 34.25$ for consistency with previous papers. From the energy-momentum tensor we can derive equations of motion. The system is decomposed into our choice of ‘field’ and ‘fluid’ parts,

$$\begin{aligned} [\partial_\mu T^{\mu\nu}]_{\text{field}} &= (\partial_\mu \partial^\mu \phi) \partial^\nu \phi - \frac{\partial V}{\partial \phi} \partial^\nu \phi \\ &= \eta U^\mu \partial_\mu \phi \partial^\nu \phi, \end{aligned} \quad (25)$$

$$\begin{aligned} [\partial_\mu T^{\mu\nu}]_{\text{fluid}} &= \partial_\mu [(\epsilon + p) U^\mu U^\nu] - \partial^\nu p + \frac{\partial V}{\partial \phi} \partial^\nu \phi \\ &= -\eta U^\mu \partial_\mu \phi \partial^\nu \phi. \end{aligned} \quad (26)$$

The parameter η sets the scale of the friction and, hence, the wall velocity.

We simulate the coupled field-fluid system using parameters familiar from Refs. [27, 29], summarised in Table I (again, for consistency with previous work, we use units where $G = T_c = 1$). The ‘weak’ and ‘weak scaled’ parameters give a phase transition strength $\alpha_{T_N} \approx 0.01$, while the ‘intermediate’ parameters give $\alpha_{T_N} \approx 0.1$.

It was hoped that ‘scaled’ forms of the ‘intermediate’ parameters could also be used, to improve the dynamic range of the simulations, but in tests using a spherically symmetric code it was found that the resulting fluid shock at $v_w = 0.44$ cannot be resolved well with our current simulation code and available resources.

From the potential (22), we can compute the surface tension σ

$$\sigma = \frac{2\sqrt{2}}{81} \frac{\alpha^3}{\lambda^{5/2}} T_c^3 \quad (27)$$

and the correlation length in the broken phase ℓ

$$\ell^2 = \frac{9\lambda}{2\alpha^2 T_c^2}. \quad (28)$$

The latent heat at the critical temperature is

$$\mathcal{L} = \frac{\alpha^2 \gamma}{\lambda^2} T_0^2 T_c^2 \quad (29)$$

and the ratio of latent heat to radiation α_T can then be written as

$$\alpha_T = \frac{\mathcal{L}}{3aT^4}. \quad (30)$$

These derived quantities, along with other relevant quantities for the simulations, are shown in Table II.

A. Gravitational waves from colliding scalar field bubbles

In Ref. [29] it was conjectured that the ω^{-1} power law seen above the peak in the gravitational wave power spectrum was the same as that produced by the envelope approximation. In this section we shall test that hypothesis.

To make the comparison as exact as possible we compare bubbles nucleated in exactly the same positions for both the field-fluid model and the envelope approximation, although we note that even for $N_b = 37$ in Ref. [29] there was no noticeable difference between power spectra when bubbles were nucleated in different positions. Again, since the envelope approximation calculation outlined above only gives the power radiated in the specified \hat{z} -direction, we repeat the envelope approximation simulation for 32 randomly selected directions uniformly distributed on the surface of the sphere. As we are directly comparing lattice simulations and envelope approximation calculations for the same configuration, random errors quoted in this section are those arising from this sampling.

In Fig. 4, we rescale the gravitational wave power spectra for the ‘weak’, ‘weak scaled’ and ‘intermediate’ phase transition parameters by the respective scalar field energy densities. This shows that the ‘weak’ and ‘weak scaled’ cases give broadly similar power spectra, lying systematically about 1σ below most points in the envelope approximation. Agreement with the ‘intermediate’ parameters is not as good, perhaps because the increased surface tension deforms the bubbles as they collide.

In Fig. 5, we instead scale the envelope approximation and compare with the actual gravitational wave power spectrum for the ‘weak scaled’ parameters. Also shown are the broken-phase correlation length ℓ and the simulation box size L , to give an indication of the limitations imposed by dynamic range. For this case, in Fig. 6 we also plot the dimensionless scalar field and fluid kinetic energy quantities:

$$\bar{U}_f = \sqrt{\frac{1}{\mathcal{V}(\bar{\epsilon} + \bar{p})} \int d^3x \tau_{ii}^f}, \quad (31)$$

$$\bar{U}_\phi = \sqrt{\frac{1}{\mathcal{V}(\bar{\epsilon} + \bar{p})} \int d^3x \tau_{ii}^\phi}. \quad (32)$$

These are compared to the equivalent quantity $\bar{U}_{\phi,\text{env}}$ computed during a run of the envelope approximation

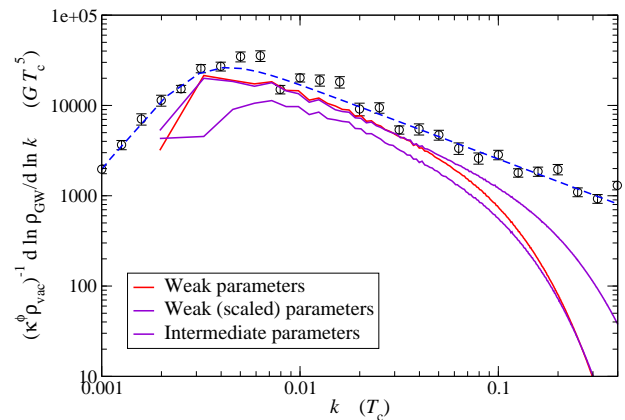


FIG. 4: Gravitational waves from colliding scalar field bubble walls. Comparison of power spectra computed by the envelope approximation (points with error bars; blue dashed line fit) and by lattice simulations with source τ_{ij}^ϕ and ‘weak’ (red curve), ‘weak scaled’ (purple curve), and ‘intermediate’ (green curve) phase transition parameters given in the main text. The resulting gravitational wave power is scaled by the scalar field gradient energy density $\kappa^\phi \rho^{\text{vac}}$, meaning all three lattice simulations are directly comparable to one envelope computation. The envelope computations were made with the same bubble positions, asymptotic wall velocity ($v_w = 0.44$), and scalar gradient energy as develops during the lattice simulation.

based on the uncollided surface area and the scalar field gradient energy. There is very good agreement between \bar{U}_ϕ and $\bar{U}_{\phi,\text{env}}$: the acceleration of the bubbles in the full simulation is seemingly of little importance to the scalar field source.

For the phase transition strengths studied here there is no evidence that the presence of fluid in front of the wall affects the power spectrum. The gravitational wave power spectrum sourced by the scalar field, shown in Figs. 4 and 5, does not change when the fluid part of the simulation is not evolved dynamically but the friction term is retained so that the wall velocity is unchanged.

B. Gravitational waves from colliding fluid shells

We now turn our attention to the form of the fluid power spectrum immediately after the bubbles have collided, and hypothesise that the gravitational wave power produced by the fluid up to this point might still be computed with the envelope approximation. The later contribution due to sound waves must then be computed separately.

The computation proceeds as before, except that in Eq. (10) the energy density is scaled by the fraction κ^f of vacuum energy that gets turned into fluid kinetic energy as the bubbles grow. While in the scalar field case in the previous section, the energy density ρ was estimated based on the surface of each bubble at collision, here we can directly measure the total fluid kinetic energy at the

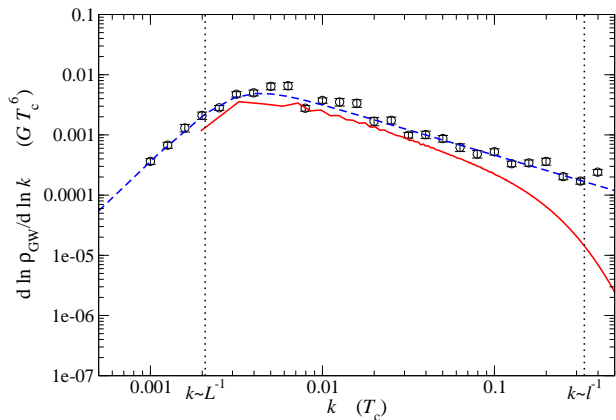


FIG. 5: As for Fig. 4, but without the scaling by $\kappa^f \rho^{\text{vac}}$, so comparison with only one lattice simulation is possible, in this case the ‘weak scaled’ simulation. The box size L and approximate wall width ℓ are shown by vertical dashed lines.

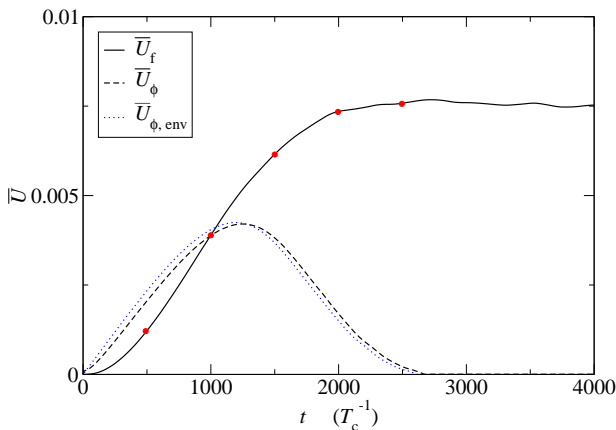


FIG. 6: Dimensionless estimates of the field and fluid energy density (\bar{U}_f and \bar{U}_ϕ) for the ‘weak scaled’ simulation (see Fig. 5), along with inferred field energy density from the corresponding envelope approximation calculation ($\bar{U}_{\phi, \text{env}}$). The red circles indicate the times at which the gravitational wave power spectrum sourced by the fluid is shown in Fig. 7.

end of the transition and use it to compute an efficiency (see Table II); this can also be computed analytically [20].

In Fig. 6 the dimensionless measure of the fluid kinetic energy density \bar{U}_f is shown, and as expected it remains approximately constant after the phase transition completes. Consequently, the acoustic waves present in the fluid continue to source gravitational waves, and in Fig. 7 the amplitude of the gravitational waves from the lattice simulation – shown in red – continues to grow after the phase transition has completed. The envelope approximation result, appropriately scaled by $\kappa^f \rho^{\text{vac}}$, is also shown.

By comparing the fluid kinetic energy at the indicated time intervals of $500/T_c$ in Fig. 6 with the succession of red curves in Fig. 7 – the fourth point and curve in particular – one can see that the envelope approximation gets

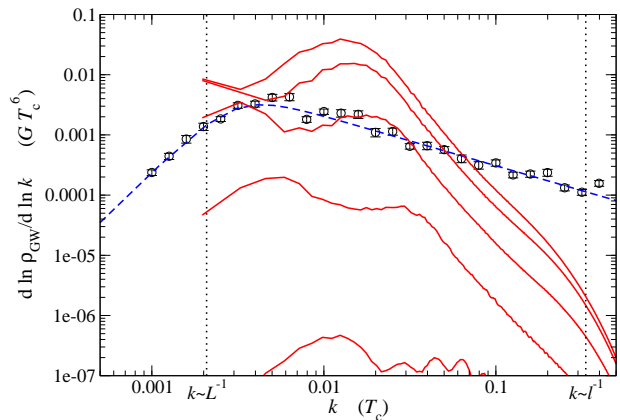


FIG. 7: Gravitational waves from colliding fluid shells for a deflagration. The envelope approximation result (blue dashed fit, black circle measurements) is scaled with the fluid energy density $\kappa^f \rho^{\text{vac}}$, with the peak value agreeing well with Eq. 2. The red curves show the gravitational wave power spectrum from the ‘weak scaled’ lattice simulation sourced by τ_{ij}^f at intervals of $500/T_c$.

the amplitude of the gravitational wave power produced by colliding fluid shells correct to within an order of magnitude at the time the fluid kinetic energy has reached its final value. The form of the power spectrum is, however, different; the peak is offset; and the total power continues to grow after this time, sourced by acoustic waves set up in the plasma after collision.

To be specific, up to the time at which the bubbles collide, there are two peaks – one closer to the infrared at $k_{\text{env}} \sim 1/R_*$, and another at higher k around the fluid shell thickness $k_{\text{shell}} \sim v_w/(R_*|v_w - c_s|)$. In this case, $k_{\text{shell}} \approx 3k_{\text{env}}$. The k_{shell} peak continues to grow, sourced by acoustic waves in the fluid. Note also that the high- k power law associated with this peak is steeper (approximately k^{-3}) than the envelope approximation. This peak continues to grow until extinguished by expansion on a timescale $1/H_*$ [29].

As a final note, in the $v_w \approx 0.44$, ‘weak parameter’ simulations discussed extensively here, the amplitude of gravitational waves sourced by the scalar field (shown in Fig. 5) and by the fluid (shown in Fig. 7) are comparable, at least as the phase transition is ending. However, in a realistic scenario, the scalar field bubble walls would be much thinner than the fluid shell, and in any case, acoustic waves (and possibly turbulence) play a more important role, at least for thermal phase transitions.

V. DISCUSSION

We have revisited previous work employing the envelope approximation to compute the gravitational wave power spectrum from colliding bubbles. The observed power laws – which are consistent with what was seen in Ref. [9] – do not depend on the nucleation rate, and it is

	Weak	Weak (scaled)	Intermediate
σ/T_c^3	1/10	1/20	$4\sqrt{2}/10$
ℓT_c	6	3	$6\sqrt{2}$
\mathcal{L}/T_c^4	9/40	9/40	9/5
α_{T_N}	0.010	0.010	0.084
$\mathcal{V}T_c^3$	4800^3	4800^3	4800^3
N_b	125	125	125
R_*	960	960	960
$\mathcal{S}T_c^2$	6.98×10^8	6.98×10^8	6.98×10^8
η/T_c	0.2	0.4	0.4
v_w	0.44	0.44	0.44
Σ	0.136	0.068	0.776
$\kappa^\phi \rho^{\text{vac}}/T_c$	0.000859	0.000430	0.00490
κ^f	0.0348	0.0348	0.195
$\kappa^f \rho^{\text{vac}}/T_c$	0.000348	0.000348	0.0164

TABLE II: Table of various derived quantities and simulation parameters. The surface tension σ , broken phase correlation length ℓ (approximately the bubble wall thickness) and phase transition strength α_{T_N} are computed from the parameters in Table I by means of Eqs. (27-30). The simulation volume \mathcal{V} and number of bubbles N_b are set for each simulation, yielding the typical bubble radius $R_* = (\mathcal{V}/N_b)^{1/3}$. The total collided ‘surface area’ \mathcal{S} can be computed given the Voronoi partition of the nucleated bubble locations. The friction parameter η determines the wall velocity v_w , chosen in each case to give a fast deflagration (such that $v_w \approx 0.44$ would be achieved if the bubbles could expand unimpeded). The scalar field gradient energy per unit area Σ is approximately proportional to σ . The scalar field energy density is then $\kappa^\phi \rho^{\text{vac}} = \Sigma \mathcal{S}/\mathcal{V}$, since the energy in the scalar field source scales only with the radius of the bubbles, whereas the fluid source scales with the volume and hence $\kappa^f \rho^{\text{vac}}$ can be computed analytically for the general case [20].

possible to reweight from simulations with simultaneous nucleation to more physical scenarios. We have no evidence that the hierarchy of bubble sizes affects the power law above the peak – the power laws are an intrinsic feature of the envelope approximation.

In addition, we compared the envelope approximation to large-scale lattice simulations of a thermal phase transition, where a scalar field expands in a plasma of light particles. The envelope approximation is a good model for the gravitational waves produced by the scalar field, although it seems to perform less well at higher surface tensions.

For gravitational waves sourced by the plasma, the envelope approximation gets the peak amplitude approximately correct, but the form of the power spectrum is incorrect. Furthermore, the subsequent acoustic and turbulent behaviour cannot be modelled at all.

This paper focused on fairly fast ($v_w = 0.44$) subsonic deflagrations. In such cases the fluid shells are very thick, about a third the radius of the bubble itself. Future

work will consider the possibility that the initial transient collision of very thin fluid shells – such as in the fine-tuned Jouguet case where $v_w \approx c_s$ – might be better described by the envelope approximation. At late times, though, the dominant sources will still be sound waves and turbulence.

It is expected that, for a viable first order electroweak-scale phase transition, the sources for which the envelope approximation would be valid – the scalar field bubble collisions, and possibly the initial fluid shell collisions – are subdominant. However, this is not necessarily the case, depending on β/H_* , or if the bubble wall runs away. Our results are valuable in any case because they represent the first comparison of the envelope approximation with alternative methods of modelling gravitational waves. They also represent an external test of the ‘gravity sector’ of the simulation code in Refs. [27, 29].

We used novel boundary conditions for our envelope approximation calculation. When the ‘spherical cutoff’ approach is used, the number of pairs of bubble interactions that must be checked grows only as N_b^2 , whereas in our hypercubic case, it grows as $27N_b^2$. Therefore, if we had adopted the standard technique, about five times as many bubbles could be simulated for the same amount of computing time.

There are important consequences for modelling the gravitational wave production from first-order phase transitions: the true peak may be shifted to higher k by up to an order of magnitude, although the amplitude will be higher; and the power laws associated with the peak may well be steeper. These effects mean care must be taken when discussing the prospects for detection at future detectors such as eLISA [5].

We conclude by reaffirming the utility of the envelope approximation for modelling the immediate aftermath of a thermal phase transition, or for situations where the fluid does not contribute (such as vacuum bubbles). For the majority of cases – where the fluid source is dominant – an analytic or at least semi-analytic method is still lacking, and direct numerical simulation is still necessary.

Acknowledgments

Our simulations made use of ‘gorina1’ at the University of Stavanger as well as the Abel cluster, a Notur facility. We acknowledge PRACE for awarding us access to resource HAZEL HEN based in Germany at the High Performance Computing Center Stuttgart (HLRS). We acknowledge useful discussions with Mark Hindmarsh, Stephan Huber, Kari Rummukainen and Anders Tranberg. Our work was supported by the People Programme (Marie Skłodowska-Curie actions) of the European Union Seventh Framework Programme (FP7/2007-2013) under grant agreement number PIEF-GA-2013-629425.

-
- [1] T. Accadia et al., in *Proceedings, 12th Marcel Grossmann Meeting on General Relativity, Paris, France, July 12-18, 2009. Vol. 1-3* (2009), pp. 1738–1742.
- [2] G. M. Harry (LIGO Scientific), *Class.Quant.Grav.* **27**, 084006 (2010).
- [3] B. P. Abbott et al. (Virgo, LIGO Scientific), *Phys. Rev. Lett.* **116**, 061102 (2016), 1602.03837.
- [4] P. A. Seoane et al. (eLISA) (2013), 1305.5720.
- [5] C. Caprini et al., *JCAP* **1604**, 001 (2016), 1512.06239.
- [6] M. Kamionkowski, A. Kosowsky, and M. S. Turner, *Phys.Rev.* **D49**, 2837 (1994), astro-ph/9310044.
- [7] R. Apreda, M. Maggiore, A. Nicolis, and A. Riotto, *Nucl. Phys.* **B631**, 342 (2002), gr-qc/0107033.
- [8] C. Grojean and G. Servant, *Phys. Rev.* **D75**, 043507 (2007), hep-ph/0607107.
- [9] S. J. Huber and T. Konstandin, *JCAP* **0809**, 022 (2008), 0806.1828.
- [10] A. Ashoorioon and T. Konstandin, *JHEP* **07**, 086 (2009), 0904.0353.
- [11] J. Kozaczuk, S. Profumo, L. S. Haskins, and C. L. Wainwright, *JHEP* **01**, 144 (2015), 1407.4134.
- [12] G. C. Dorsch, S. J. Huber, and J. M. No, *Phys. Rev. Lett.* **113**, 121801 (2014), 1403.5583.
- [13] M. Kakizaki, S. Kanemura, and T. Matsui, *Phys. Rev.* **D92**, 115007 (2015), 1509.08394.
- [14] L. Leitao and A. Megevand, *JCAP* **1605**, 037 (2016), 1512.08962.
- [15] P. Schwaller, *Phys. Rev. Lett.* **115**, 181101 (2015), 1504.07263.
- [16] J. Jaeckel, V. V. Khoze, and M. Spannowsky (2016), 1602.03901.
- [17] P. S. B. Dev and A. Mazumdar, *Phys. Rev.* **D93**, 104001 (2016), 1602.04203.
- [18] A. Kosowsky, M. S. Turner, and R. Watkins, *Phys.Rev.* **D45**, 4514 (1992).
- [19] A. Kosowsky and M. S. Turner, *Phys.Rev.* **D47**, 4372 (1993), astro-ph/9211004.
- [20] J. R. Espinosa, T. Konstandin, J. M. No, and G. Servant, *JCAP* **1006**, 028 (2010), 1004.4187.
- [21] C. Caprini, R. Durrer, and G. Servant, *Phys. Rev.* **D77**, 124015 (2008), 0711.2593.
- [22] C. Caprini, R. Durrer, T. Konstandin, and G. Servant, *Phys.Rev.* **D79**, 083519 (2009), 0901.1661.
- [23] R. Jinno and M. Takimoto (2016), 1605.01403.
- [24] A. Kosowsky, A. Mack, and T. Kahniashvili, *Phys. Rev.* **D66**, 024030 (2002), astro-ph/0111483.
- [25] T. Kahniashvili, A. Kosowsky, G. Gogoberidze, and Y. Maravin, *Phys. Rev.* **D78**, 043003 (2008), 0806.0293.
- [26] C. Caprini, R. Durrer, and G. Servant, *JCAP* **0912**, 024 (2009), 0909.0622.
- [27] M. Hindmarsh, S. J. Huber, K. Rummukainen, and D. J. Weir, *Phys.Rev.Lett.* **112**, 041301 (2014), 1304.2433.
- [28] J. T. Giblin and J. B. Mertens, *Phys.Rev.* **D90**, 023532 (2014), 1405.4005.
- [29] M. Hindmarsh, S. J. Huber, K. Rummukainen, and D. J. Weir, *Phys. Rev.* **D92**, 123009 (2015), 1504.03291.
- [30] S. Weinberg, *Gravitation and Cosmology* (Wiley, New York, 1972).
- [31] C. Caprini, R. Durrer, and X. Siemens, *Phys.Rev.* **D82**, 063511 (2010), 1007.1218.
- [32] S. R. Coleman, *Phys. Rev.* **D15**, 2929 (1977), [Erratum: *Phys. Rev.*D16,1248(1977)].
- [33] C. G. Callan, Jr. and S. R. Coleman, *Phys. Rev.* **D16**, 1762 (1977).
- [34] A. D. Linde, *Nucl. Phys.* **B216**, 421 (1983), [Erratum: *Nucl. Phys.*B223,544(1983)].
- [35] K. Enqvist, J. Ignatius, K. Kajantie, and K. Rummukainen, *Phys. Rev.* **D45**, 3415 (1992).
- [36] K. Kajantie and H. Kurki-Suonio, *Phys.Rev.* **D34**, 1719 (1986).
- [37] J. Ignatius, K. Kajantie, H. Kurki-Suonio, and M. Laine, *Phys.Rev.* **D49**, 3854 (1994), astro-ph/9309059.
- [38] J. Ignatius, K. Kajantie, H. Kurki-Suonio, and M. Laine, *Phys.Rev.* **D50**, 3738 (1994), hep-ph/9405336.
- [39] H. Kurki-Suonio and M. Laine, *Phys.Rev.* **D51**, 5431 (1995), hep-ph/9501216.
- [40] H. Kurki-Suonio and M. Laine, *Phys.Rev.* **D54**, 7163 (1996), hep-ph/9512202.
- [41] H. Kurki-Suonio and M. Laine, *Phys.Rev.Lett.* **77**, 3951 (1996), hep-ph/9607382.